Remote Sensing of Environment 201 (2017) 47–56

Contents lists available at ScienceDirect

Remote Sensing of Environment

journal homepage: www.elsevier.com/locate/rse

Sentinel-2 MultiSpectral Instrument (MSI) data processing for aquatic science applications: Demonstrations and validations

N. Pahlevan[a,b,*], S. Sarkar[a,b], B.A. Franz[a], S.V. Balasubramanian[a,c], J. He[c]

[a] NASA Goddard Space Flight Center, 8800 Greenbelt Road, Greenbelt, MD 20771, USA
[b] Science Systems and Applications, Inc., 10210 Greenbelt Road, Suite 600, Lanham, MD 20706, USA
[c] University of Maryland, Department of Geographical Sciences, College Park 20740, USA

ARTICLE INFO

Keywords:
Sentinel-2A
Atmospheric correction
Aquatic science applications
Calibration/validation

ABSTRACT

The European Space Agency's Sentinel-2A mission with the MultiSpectral Instrument (MSI) onboard was launched in 2015, initiating a new era in high-to-moderate-resolution (i.e., 10 to 60 m) imaging of Earth's resources. This manuscript describes the implementations of MSI processing into the SeaWiFS Data Analysis System (SeaDAS) and provides qualitative and quantitative analyses of remote sensing reflectance products (R_{rs}), which are essential in the retrievals of near-surface concentrations of water constituents in aquatic systems. In situ validations and intercomparisons of MSI-derived R_{rs} products with those derived from Landsat-8's Operational Land Imager (OLI) both indicated reasonable products in coastal/inland waters. Following vicarious calibrations using reference in situ water-leaving radiances, the overall absolute relative differences and the root mean squared differences (RMSD) found for the matchup analyses were, < 7% and < 0.0012 1/sr, respectively, for the blue and green bands. With preliminary indications of consistency with the OLI products and very good agreements with in situ data, a time-series plot of total suspended solids (TSS) product derived from both missions was produced and analyzed for an inland system. It is surmised that frequent moderate-to-high resolution R_{rs} products from the combined Sentinel-2A (and B) and Landsat-8 missions are now available to the science/user community for developing algorithms suited for coastal/inland waters. Nonetheless, further research needs to be dedicated to a) improving atmospheric corrections over bodies of waters rich in dissolved organic matter or suspended particles, b) mitigating the impact of haze- or sea surface-reflected solar radiations at low solar zenith angles, and c) minimizing image artifacts to maximize the use of multi-mission products.

1. Introduction

The Sentinel-2A mission carries the MutiSpectral Instrument (MSI), which measures the reflected solar spectral radiances in 13 spectral bands ranging from the visible to the shortwave infrared (SWIR) bands (Drusch et al., 2012). The European Space Agency's Copernicus program has planned a series of Sentinel-2 satellites with 5-day revisit time over land and coastal areas. The 5-day revisit time is met with two MSIs aboard Sentinel-2A and Sentinel-2B. With a seven-year lifetime design, the existing twin satellites are planned be replaced in 2022–2023 timeframe by new identical missions taking the data record to the 2030 timeframe. The primary purpose is to enable regular monitoring of global landuse/landcover change at local/regional/national/global scales. It is, however, expected that the MSI can also open opportunities for mapping near-surface water constituents, including the concentrations of total suspended solids (TSS) and chlorophyll-*a* (Chl) and potentially the absorption by colored dissolved organic matter (CDOM), in nearshore coastal and inland waters. This is because MSI is very similar in design and requirements to the Operational Land Imager (OLI) onboard Landsat-8 (Drusch et al., 2012; Segl et al., 2015), which has been demonstrated to provide high-quality aquatic science products over coastal/inland waters (Franz et al., 2015; Vanhellemont and Ruddick, 2015). However, comparing to the OLI, MSI offers even more spectral measurements within the near-infrared (NIR) region (D'Odorico et al., 2013). These additional spectral bands are advantageous over optically complex coastal/inland waters (IOCCG, 2000; Moses et al., 2009) and will provide opportunities for enhanced retrievals of TSS and Chl in hypertrophic, CDOM-rich (Kutser et al., 2016; Toming et al., 2016), or extremely turbid waters (Lee et al., 2016; Liu et al., 2017; Nechad et al., 2010). Furthermore, with 10 and 20 m ground sampling distances (GSDs) in most of the visible and all of the NIR bands, MSI should allow a) for more valid observations (i.e., pure water pixel) in nearshore waters and b) for mapping water quality conditions in smaller inland bodies of waters (e.g., narrow rivers and streams). Table 1 contains the

* Corresponding author at: NASA Goddard Space Flight Center, 8800 Greenbelt Road, Greenbelt, MD 20771, USA.
E-mail address: nima.pahlevan@nasa.gov (N. Pahlevan).

http://dx.doi.org/10.1016/j.rse.2017.08.033
Received 4 May 2017; Received in revised form 18 August 2017; Accepted 25 August 2017
Available online 08 September 2017

Table 1
The nominal band centers, bandwidths, spatial resolution and the signal-to-noise ratios of Sentinel-2 MSI. Also included are the corresponding characteristics of OLI for comparisons. The mean TOA radiances (L_t) are in units of $w\,m^{-2}\mu^{-1}\,sr^{-1}$.

Nominal band centers (nm)											
MSI	444	497	560	664	704	740	783	843	865	1613	2200
OLI	443	482	561	655	NA	NA	NA	NA	865	1609	2201
Nominal bandwidths (nm) @ full width half maximum (FWHM)											
MSI	20	55	35	30	15	15	15	115	20	90	175
OLI	20	65	60	40	NA	NA	NA	NA	30	85	190
Spatial resolution (m)											
MSI	60	10	10	10	20	20	20	10	20	20	20
OLI	30	30	30	30	NA	NA	NA	NA	30	30	30
Signal-to-noise ratio (SNR)											
MSI	439	102	79	45	45	34	26	20	16	2.8	2.2
OLI	284	321	223	113	NA	NA	NA	NA	45	10.1	7.4
L_t	51.2	36.6	21.1	9.1	7.0	5.2	4.2	2.9	2.45	0.11	0.025

list of GSDs (hereafter is referred to as "spatial resolution") for all of the MSI spectral bands applicable in deriving R_{rs} products, defined as the ratio of water-leaving radiance to the total downwelling irradiance just above water, and the corresponding aquatic science products (e.g., Chl).

The objective of this study is to provide and evaluate MSI-derived R_{rs} products whose quality is critical for the retrieval of biogeochemical properties and/or inherent optical properties of water column in nearshore coastal and inland areas. This manuscript provides analyses of the radiometric fidelity of MSI (Section 2), the implementation of Sentinel-2A data processing in the SeaWiFS Data Analysis System (SeaDAS) (Section 3), an assessment of product quality (Section 4), the vicarious enhancements of MSI's absolute radiometric calibration and the impacts on R_{rs} products (Section 5), and finally, a demonstration of temporal TSS variability derived from Landsat-8-Sentinel-2 constellation in inland waters (Section 6). The manuscript ends with discussions and directions for future multi-mission product developments (Section 7) followed by a summary and conclusion.

2. Radiometric analysis

The radiometric quality of image products is critical for aquatic science applications as, over these dark targets, the majority of the signal reaching the sensor is comprised of unwanted atmospheric signal (Gordon, 1990). The MSI is a push broom imager with linear arrays of detectors laid out on the focal plane in 12 staggered modules forming the entire image swath, i.e., ~290 km (Drusch et al., 2012; Meygret et al., 2009). The calibrated top-of-atmosphere (TOA) reflectance products are provided to the science/user community at its native spatial resolution in 100 km × 100 km tile formats, termed Level-1C (L1C) products. The imaging geometry information, including the view zenith angle (VZA), view azimuth angle (VAA), solar zenith angle (SZA), and solar azimuth angles (SAA), are, however, stored in 5 km × 5 km grids (Meygret et al., 2009).

The signal-to-noise (SNR) requirements for typical radiances over land targets are given in Drusch et al. (2012). To examine MSI on-orbit radiometric performance over bodies of water, an assessment of its SNR was carried out using > 30 L1C images over spatially uniform and clear waters. Fig. 1 shows the mean SNR computed by taking the average of locally estimated SNRs using the ratio of mean (μ) to standard deviation (σ), i.e., μ/σ. The calculations were performed for 7 × 7-element windows in a similar fashion as performed for OLI SNR calculations

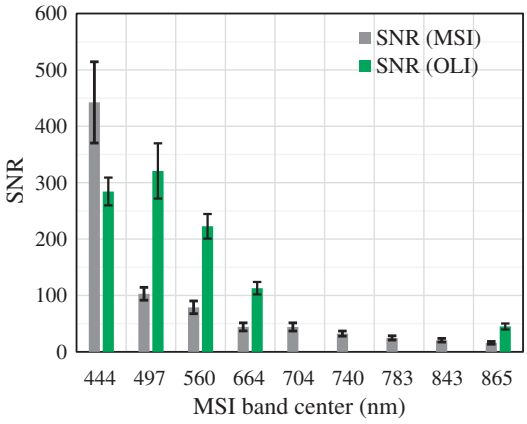

Fig. 1. The image-derived signal-to-noise ratio (SNR) of the MultiSpectral Instrument (MSI) calculated over clear, uniform bodies of water. The SNRs are computed for the native spatial resolution of MSI spectral bands (Table 1) for typical radiances found over clear water bodies. While, in general, the MSI SNRs are comparable to those of OLI (Pahlevan et al., 2014b), the OLI seems to offer higher SNRs at its native 30 m resolution (see Table 1). To allow for comparable OLI-MSI product qualities, the MSI products may need to be aggregated.

(Pahlevan et al., 2014b). The computed SNRs are compared with the corresponding SNR values for the OLI. For fair intercomparisons, the OLI's SNRs were scaled (Pahlevan et al., 2014a) to the mean TOA radiance levels utilized in this study (Table 1). The mean SNRs calculated for the MSI's native spatial resolutions for mean radiances (L_t; $w\,m^{-2}\mu^{-1}\,sr^{-1}$) observed at mean SZA of 49° are tabulated in Table 1.

It is inferred that the OLI's SNR for the three visible bands (497, 560, and 664 nm) are 2X to 3X better than those of MSI, whereas, MSI SNR@ 444 nm is 40% higher than that of the OLI. Recognizing that the SNR is proportional to the square root of the area of a pixel (Schott, 2007), it can be surmised that aggregated 20 or 30 m MSI bands should offer similar or better radiometric quality in the aforementioned three visible bands (see Section 6). Similarly, aggregated 60 m OLI 443 nm images (Table 1) offer 30% higher SNR in the corresponding MSI band. Therefore, the overall radiometric quality of MSI and OLI products is comparable, and both are found to offer more precise measurements than those of the heritage Landsat missions over aquatic systems (Franz et al., 2015; Gerace et al., 2013; Hu et al., 2012; Pahlevan and Schott, 2013). Note also that OLI's SNRs in the SWIR bands are 3X to 4X better

than those of MSI (Table 1). These differences in the noise level will have implications on the performance of atmospheric correction (Wang and Wei, 2012). In general, one should keep in mind that the on-orbit SNR performance of OLI is 2X to 3X better than the requirements (Irons et al., 2012; Pahlevan et al., 2014b) due to design trades for minimizing non-uniformities (striping) (Knight, 2017).

3. Methodology

For the implementation of the atmospheric correction, we followed the standard methodology introduced in Gordon and Wang (1994) in which the TOA reflectance is formulated as below

$$\rho_t(\lambda) = t\rho_w(\lambda) + \{\rho_r(\lambda) + \rho_a(\lambda) + \rho_{ar}(\lambda)\}$$

where t is the diffuse transmission, ρ_r is the Rayleigh reflectance in the absence of aerosol, ρ_a is the aerosol radiance, and ρ_{ar} is the radiance arising from Rayleigh-aerosol multiple scattering, and ρ_w is the water-leaving reflectance just above water, which can readily be converted to R_{rs} (Mobley et al., 2016). The goal is to retrieve R_{rs} which is the critical parameter for the retrievals of the inherent optical properties (IOP) and the biogeochemical variables. Note that in the above notation, we have dropped contributions from the sunglint and whitecaps for brevity. Also, the above equation can be interchangeably expressed in radiance domain (L). A vector radiative transfer simulation (Ahmad and Fraser, 1982) was performed, in combination with the MSI spectral response functions, to develop the common aerosol and Rayleigh look-up-tables used as part of the SeaWiFS Data Analysis System (SeaDAS). Per-pixel (10, 20, and 60 m) and per-band viewing angle coefficients (i.e., VZA and VAA) were re-created using coarse-resolution (5 km × 5 km) angle information provided in metadata files (Gatti and Bertolini, 2013). The per-pixel reconstruction of angle coefficients was carried out in a few steps: convert the given angles to observations of directions to the Sentinel-2A spacecraft (i.e., line of sight), reconstruct the orbit from the viewing angles and calculate the time for each grid cell, use the calculated observation times to construct a line/sample versus time model for each band and detector module, and generate the angle files for each spectral band (see Appendix A for a detailed description provided by James Storey and the corresponding code provided as supplementary material in Appendix B). Therefore, the viewing angle coefficients for 10, 20, and 60 m resolution bands are available in the processing. On the other hand, the fine-resolution solar angles (SZA and SAZ) were created simply by replicating the course-resolution angles.

A full description of NASA's standard atmospheric correction process is given in (Mobley et al., 2016). The process begins with removing the Rayleigh contribution using ancillary data (including digital elevation models) and pre-computed LUTs, followed by the aerosol removal. The band ratio of Rayleigh-corrected radiance, i.e., $L_t - L_r = L_r + L_a$, for two bands where $R_{rs} \approx 0$, is then computed and used to infer an aerosol type. This band ratio is extrapolated to the visible bands and subtracted from the Rayleigh-corrected radiance. Due to non-negligible water-leaving radiances in the NIR band (Siegel et al., 2000) in most coastal/inland waters, we allow utilizations of the iterative NIR-signal removal method (Bailey et al., 2010) that is currently available in SeaDAS. Further, for simplicity in processing, we resampled the 10 m resolution bands to a common grid with 20 m grid cells via arithmetic averaging. The 444 nm band data (at 60 m) are replicated for underlying 20 m grid cells. In addition, similar to the OLI processing (Franz et al., 2015), to minimize the noise effects, the MSI ρ_t images were smoothed using a 9 × 9-element (180 m × 180 m) averaging filter. Effectively, the 443 nm band is averaged by a 3 × 3-element window and the other visible bands are averaged by an 18 × 18-element window. For intercomparisons with OLI products (Section 4), OLI products were smoothed using a 6 × 6-element window.

The performance of the atmospheric correction was further evaluated against the in situ radiometric measurements made at the ocean color component of the AErosol RObotic NETwork (AERONET-OC) sites (Zibordi et al., 2006). For the image statistics, median R_{rs} computed for 7 × 7-element windows was used. The 3 × 3-element center pixels were discarded to avoid adjacency effects induced by the AERONET-OC platforms (Pahlevan et al., 2016). Note further that SeaDAS applies a broadband to narrowband (10 nm) conversion (Wang et al., 2001) to create R_{rs} values centered at band centers specified in Table 1. We examined three different band combinations for the removal of aerosol contributions to evaluate the relative performances (Franz et al., 2015; Wang and Shi, 2007). These include the 865–1613 nm, 865–2200 nm, and 1613–2200 nm. The in situ AERONET-OC data (Zibordi et al., 2009) collected within a +/− 1 h interval of satellite overpasses were considered for matchup analyses. This is a more restricted matchup analysis than that suggested for global ocean color missions (Bailey and Werdell, 2006), to accommodate the dynamic nature of the exclusively coastal in situ locations employed.

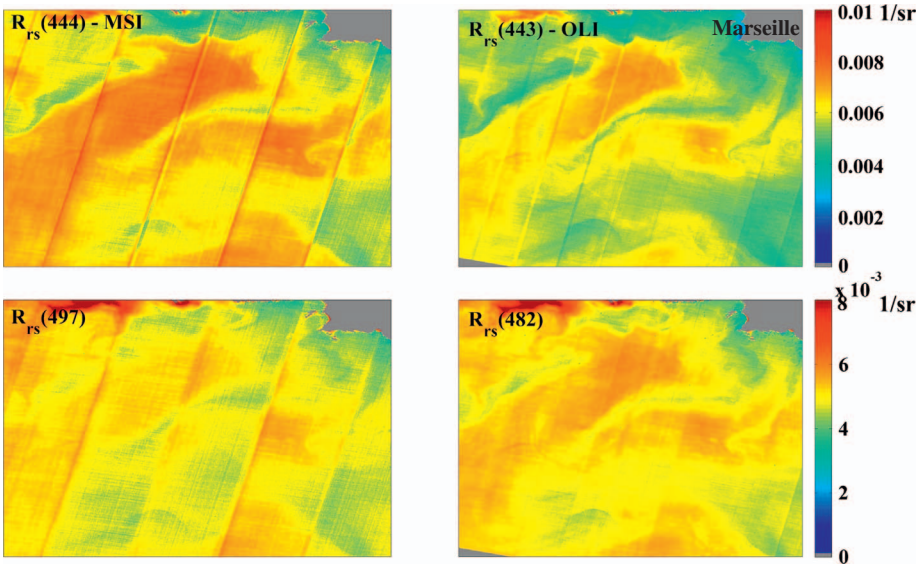

Fig. 2. The MSI-derived R_{rs} in the blue bands compared to those derived from near-simultaneous OLI data products over clear waters of northern Mediterranean Sea, South France (2016/08/23). In general, our SeaDAS-processed MSI products yield very comparable results to those of OLI. The primary discrepancies are the differences in the overall brightness and artifacts more pronounced in the MSI products than in the OLI products. Note that the mean view zenith and solar zenith angles are (10°, 30°) and (2°, 37°) for MSI and OLI, respectively. The differences in imaging geometries can explain some of the differences in the two products. (For interpretation of the references to color in this figure legend, the reader is referred to the web version of this article.)

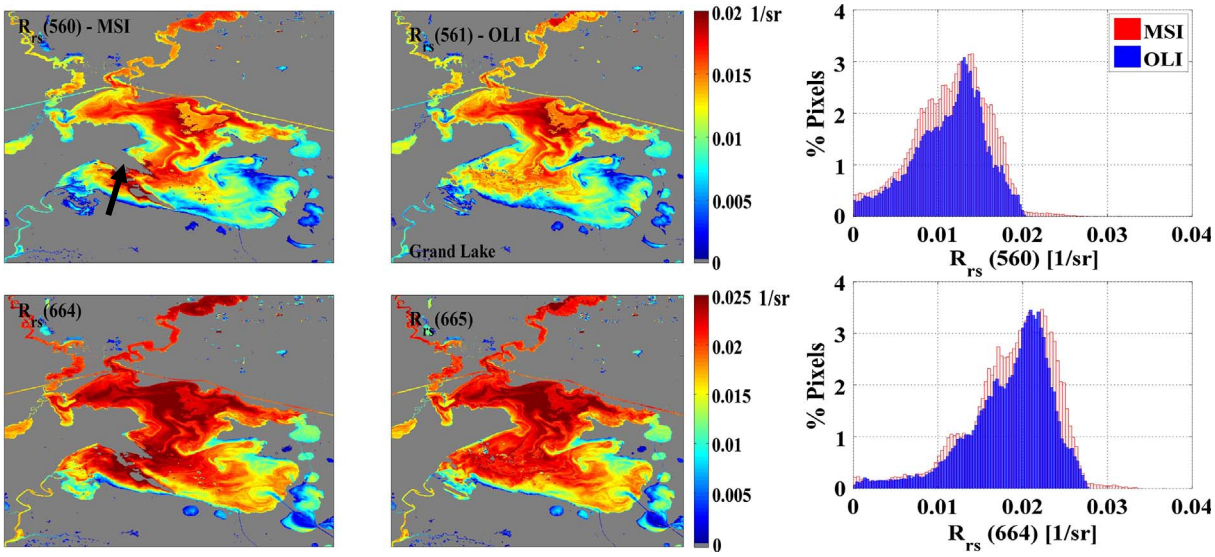

Fig. 3. The MSI-derived R_{rs} (560 nm) and R_{rs}(664 nm) are shown for the Grand Lake (Louisiana, USA). The images were acquired on Feb 10th 2017 (Grand Lake). The fine spatial details of in-water optically active components are noticeable in both MSI and OLI image products over Grand Lake. Note the presence of patches of clouds in the MSI products (indicated with an arrow). The histograms further indicate the level of coherence in R_{rs} products.

4. Results

4.1. Qualitative analysis

The MSI-derived R_{rs} products are shown alongside the OLI products (Franz et al., 2015) in Figs. 2–4. The image pairs are taken near-simultaneously, i.e., within 20–25 min, thus, similar aerosol/atmospheric conditions can be assumed. The Landsat-8 and Sentinel-2A are placed in morning orbits at different altitudes (nominal 705 and 786 km, respectively), which allow for frequent near-simultaneous nadir overpasses (Cao et al., 2004). While the MSI L1C data are processed "as-is" (https://scihub.copernicus.eu), the OLI TOA reflectance data (https://earthexplorer.usgs.gov) have undergone vicarious calibrations and corrections for residual instrument across-track non-uniformities (Pahlevan et al., 2017b). Thus, OLI products may be regarded as references against which MSI products are evaluated. The OLI vicarious calibration gains were derived using in situ radiometric observations (Franz et al., 2007) made at the Marine Optical Buoy (MOBY) (Clark et al., 2003) and non-uniformity corrections were obtained through intercomparisons with ocean color data products (see Fig. 8 in Pahlevan et al., 2017b). The aerosol removal for both OLI and MSI has been carried out using the NIR-SWIR band combination, i.e., 865–1609 nm or 865–1613 nm (Table 1). Fig. 2 illustrates the R_{rs} products (blue bands) acquired on Aug 23rd 2016 over the northern Mediterranean Sea (Southern France). Overall, it is found that our processing system produces MSI-derived products similar to those of OLI. With < 30-minute time difference in the acquisition time, all the sharp frontal regions are well captured in both datasets at nearly the same locations.

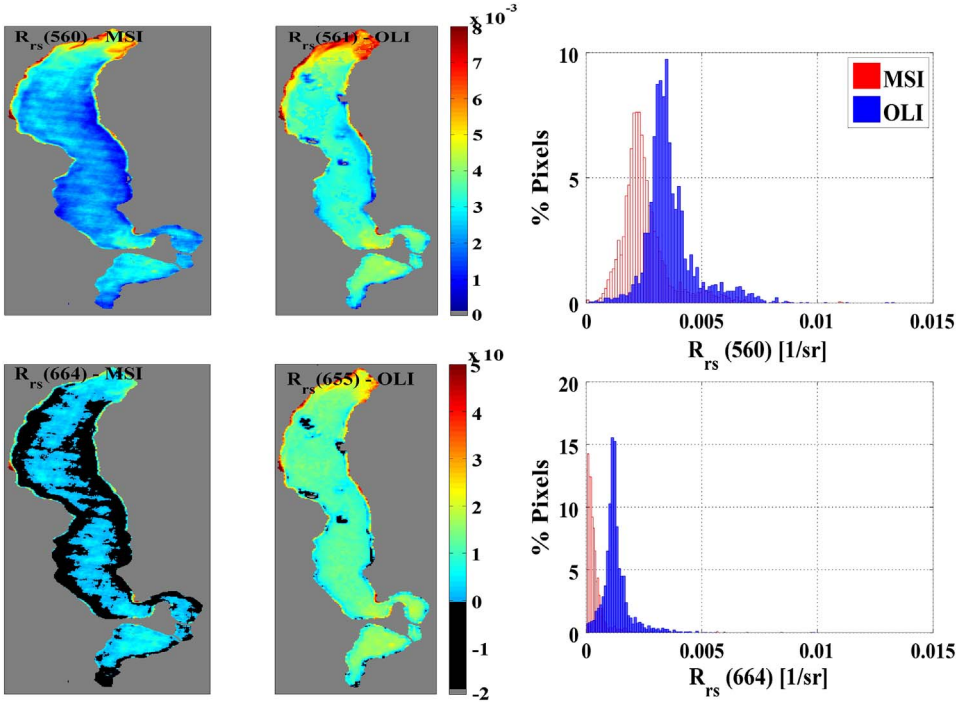

Fig. 4. The MSI-derived R_{rs} (560 nm) and R_{rs}(664 nm) are shown for Ratzeburger See (Germany). The images were acquired on March 28th 2017. Spatially uniform waters are captured by the two sensors. Few patches of clouds are present in OLI products. The lower R_{rs} values are evident in the MSI products. In particular, negative retrievals (indicated in black color) for R_{rs}(664) are noticeable near the shorelines. The histograms further demonstrate the discrepancies in the range of retrievals. Note that the OLI products have undergone vicarious calibration and across-track non-uniformity corrections (Pahlevan et al., 2017b) whereas MSI imagery were processed "as-is".

There are, however, two primary cautions worth discussing: a) the MSI overall brightness for the blue bands seem slightly different (< 30%) than that of the OLI products and b) the presence of image artifacts, which is more pronounced in MSI products for this example. The latter issue is attributed to a combination of potential instrument artifacts (e.g., non-uniformity across track or within each detector module (Pahlevan et al., 2017b)) and inaccurate removals of sea surface reflection. For this example, the differences in the mean view zenith and solar zenith angles of MSI and OLI, i.e., (VZA, SZA) = (10°, 30°) and (2°, 37°), respectively, may contribute to the apparent discrepancies in these products. Also, the differences in the relative magnitudes in the 497 nm band may be attributed to the differences in the spectral bands of MSI and OLI (Table 1). Such differences in the 444 nm band, however, are expected to be very minimal (see Section 6 for discussions). Further, differences in the absolute calibrations of the NIR and SWIR bands used in the aerosol removal process may also contribute to the differences and the observed banding effects (Pahlevan et al., 2017a). Fig. 3 shows red-green R_{rs} products derived over Grand Lake (Louisiana, USA), whose optical regime seems to be dominated by significant amount of TSS. The fine in-water features are captured in both OLI and MSI image products. It can clearly be seen that the two sets of products allude to similar magnitudes of upwelling radiance over such highly turbid systems. This can also be inferred from the frequency distributions generated by re-mapping both products to 60 m grid cells. Note that the clouds in Sentinel-2A products (indicated with an arrow) may contribute to apparent differences in these products. In contrast, the data products over Ratzeburger See are found to differ by ~20–30% in the green band and ~2× in the red band (Fig. 4). These relative differences are equal to absolute differences of 0.001 to 0.002 (1/sr). The negative retrievals are also highlighted in black color for the MSI-derived $R_{rs}(664)$. The data range in OLI and MSI products is noticeably different for both green and red products. Such apparent differences in products (Fig. 3 versus Fig. 4) can likely be attributed to inherent differences in a) the optical regimes of these two aquatic systems, i.e., one is highly turbid and the other is dominated by absorbing components, b) the atmospheric conditions, c) the imaging geometries, and d) the sensor performances. In general, the algorithm- and/or sensor-related shortfalls require further cautions over "darker" aquatic systems (e.g., boreal lakes). In Section 5, vicarious calibration gains provided will improve some of the existing biases in MSI-derived products.

The three qualitative intercomparisons were presented to furnish background information on what to anticipate when creating multi-mission products. Overall, while discrepancies may exist, products generated via SeaDAS show comparable MSI-OLI R_{rs} products.

4.2. In situ validations

For a more quantitative validation of the MSI-derived R_{rs} products, > 250 cloud-free scenes over 15 AERONET-OC sites were identified until mid August 2017. Due to the scarcity of the AERONET-OC measurements within ± 1 hour of Sentinel-2A overpasses, the number of matchups was reduced to 65 (25% of the total). Most of the valid matchups were found for the Venise, LISCO, Palgrunden, and Wave_CIS. Few data points were also obtained from Gloria, Galata, and Thornton. Fig. 5 illustrates the scatterplots associated with the matchups. The root-mean-squared differences (RMSD), the relative differences (RD), and biases are computed as below

$$RMSD(\lambda) = \left(\frac{1}{N} \sum_{1}^{N=65} R_{rs(i)}^{MSI(\lambda)} - R_{rs(i)}^{AERONET(\lambda)} \right)^{1/2}$$

$$RD(\lambda) = \frac{1}{N} \sum_{i=1}^{N=65} \frac{R_{rs(i)}^{MSI(\lambda)} - R_{rs(i)}^{AERONET(\lambda)}}{R_{rs(i)}^{AERONET(\lambda)}} \times 100$$

$$Bias(\lambda) = \frac{1}{N} \sum_{i=1}^{N=65} R_{rs(i)}^{MSI(\lambda)} - R_{rs(i)}^{AERONET(\lambda)}$$

where λ denotes MSI or AERONET-OC spectral bands. With the 65 Sentinel-2A matchups, it is evident that our implementation has produced reasonable R_{rs} products when the NIR-SWIR band combination is applied. The RMSDs range from 0.0006 to 0.0019 1/sr for this band combination. Similar to the findings in Pahlevan et al. (2017b), the SWIR-only method yields significant invalid (negative) retrievals in the blue and red bands. Calculating SNRs for the band ratios of the SWIR bands further indicated very low radiometric performances, i.e., 1.5:1. This is nearly half of the SNR for the NIR-SWIR ratios. Over these mostly moderately turbid coastal waters, the noisy SWIR detectors, which yield noisy observed Rayleigh-corrected band ratios, are deemed to be the prime cause of the failure in the atmospheric correction (Wang and Wei, 2012). Note that uncertainties in band combinations that are close in spectral distance have larger impacts on R_{rs} retrievals than the ones that are distant (see Fig. 10 in Pahlevan et al., 2017a). In addition, the 1613–2200 band combination is less sensitive to changes in aerosol types common over coastal and inland areas (Pahlevan et al., 2017a).

On the other hand, it is found that the 865–1613 nm method leads to better agreements in the blue bands than that of the 865–2200 nm approach. This is attributed to the noisier observations in the 2200 nm channel than those in the 1613 band (Table 1). According to these findings, the NIR or SWIR bands are likely to have minimal (or no) calibration biases making them suitable for the atmospheric correction of the MSI data (Franz et al., 2015). The existing biases in the visible bands will likely be removed after vicarious calibration (see Section 5).

Table 2 provides further details on the matchup analyses indicating that MSI yields higher R_{rs} in the blue and lower in the red channel. The mean biases for 865–1613 case are 0.00075, 0.000659, − 0.00031, and − 0.00039 1/sr in the 444, 497, 560, and 664 nm, respectively. The largest slope corresponds to R_{rs} (444), which suggests noisy retrievals primarily due to imperfect aerosol models (see Section 6) and potentially signal-dependent radiometric responses.

5. Vicarious calibration

The results presented thus far denote potential differences/biases in MSI-derived R_{rs} products. Here, we utilize in situ radiometric observations made at the BOUSSOLE site (Antoine et al., 2008a; Antoine et al., 2008b) to derive preliminary vicarious calibration gains to improve overall radiometric quality of MSI data products (Franz et al., 2007; Gordon, 1998). The Sentinel-2A images over the Marine Optical Buoy (MOBY) were found unusable for such an effort due to either hazy atmospheric conditions or unavailability of in situ data. Seven clear MSI scenes were identified for the vicarious calibration over the BOUSSOLE site. Only four scenes, however, passed the spatial uniformity test and were used in the final gain calculations. The water-leaving radiances were supplied as input to the SeaDAS vicarious calibration scheme (Franz et al., 2007) to derive the gains. The mean vicarious calibration gains and the corresponding standard deviations (1-sigma) are tabulated in Table 3. Note that these gains are the average gains derived using both NIR-SWIR band combinations used in the aerosol correction (see Section 6 for further discussions).

Fig. 6 illustrates the scatterplot associated with the matchup analyses (N = 65) after implementing the vicarious calibration gains. The plot includes only the results associated with the 865–1613 nm band combination that was found to produce the most robust results in the previous section. It is evident that in the absence of statistically robust vicarious calibration work, the derived gains provide significant improvements in the R_{rs} products by minimizing the biases found for the recorded MSI data (Fig. 5 and Table 2). This can be inferred by inspecting RD and bias values given in Tables 2 and 3.

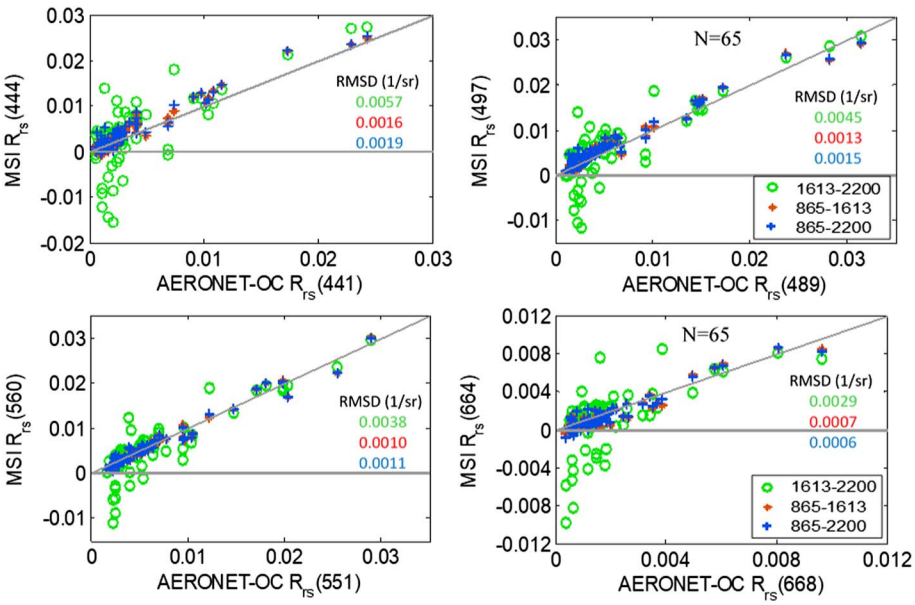

Fig. 5. Scatterplot of AERONET-OC $R_{rs}(\lambda)$ measurements versus $R_{rs}(\lambda)$ derived from Sentinel-2A (MSI) processed via SeaDAS. Different panels correspond to the performances for the four visible bands (i.e., 444, 497, 560, and 664 nm). The satellite matchups (N = 65) were limited to valid observations acquired within a ± 1 h of in situ measurements. The SWIR-only band combination shows poor performances while 865–1613 yields best results.

6. Application to temporal studies

To demonstrate and evaluate the utility of a consistent Landsat-8-Sentinel-2A data product record after vicarious calibrations, here, we show a time-series of the total suspended solids (TSS) products. To do so, an empirical TSS algorithm (Nechad et al., 2010) was implemented in SeaDAS and applied to OLI and MSI images over Lake Mead (Nevada, USA). Lake Mead was chosen because of the recent reports of harmful algal blooms and frequent cloud-free images (n = 85). Fig. 7 shows an example of an OLI-derived TSS product (left) together with a time-series plot (starting from April 2013). The plot corresponds to TSS values averaged over an area in lake's central basin. While the algorithm may not provide accurate estimations of TSS in Lake Mead, the derived products clearly capture temporal variability and potential anomalies in water conditions. The overall consistency in products can also be inferred from subsequent data points. In mid-2015, the MSI-derived products begin to fill the gaps in OLI products (every 16 days) and increase observation frequencies. This example clearly shows the potential of OLI-MSI products for use in future monitoring practices. Note that the availability of MSI products significantly increases from mid-2016.

Table 3
The preliminary vicarious calibration gains derived using the in situ observations at the BOUSSOLE site (Antoine et al., 2008b).

Band (nm)	444	497	560	664	704	740	783
Gains	0.989	0.9877	1.02133	1.006	1.0266	1.0048	0.97701
Standard deviation	0.0128	0.0165	0.0151	0.011	0.0173	0.021	0.0018

7. Discussion

Throughout this manuscript, we have demonstrated that high-quality R_{rs} products from the MSI L1C products can be produced from the SeaDAS package. Although the quality of R_{rs} products requires further community-wide validations to ensure performances under various conditions, the statistical analyses tabulated in Table 4 indicate very good performances of MSI when compared to the previously published ocean color matchup analyses for products derived from the Moderate Resolution Imaging Spectroradiometer (MODIS) (Goyens et al., 2013; Zibordi et al., 2009).

The large uncertainties in ocean color (e.g., MODIS) matchups may partially be related to inter-pixel spatial variability and adjacency

Table 2
The matchup analyses and the corresponding metrics calculated for three different aerosol correction methods, including 865–1613, 865–2200, and 1613–2200. The analyses are provided for all the visible bands for which comparable in situ AERONET-OC measurements are available. It is found that the NIR-SWIR band combination yields R_{rs} products reasonably consistent with in situ data. Relatively high biases, however, do exist for these retrievals (see Table 4 for improvements). Noisy retrievals are believed to be attributed to sensor noise, aerosol removal, and differences in the spectral bands of MSI and AERONET-OC radiometers.

Band combination	*RD (%)*	*RMSD (1/sr)*	Slope	Intercept	Bias (1/sr)	R^2
444						
1613_2200	-28.3	0.0057	1.68	-0.0028	-0.0001	0.52
865_1613	16.1	0.0016	1.14	0.000178	0.000749	0.95
865_2200	30.4	0.0019	1.14	0.000303	0.000874	0.92
497						
1613_2200	-9.5	0.0045	1.27	-0.00161	-6.2E-05	0.68
865_1613	17.1	0.0013	1.01	0.000655	0.000659	0.97
865_2200	22.7	0.0015	0.99	0.000785	0.00076	0.96
560						
1613_2200	-31.4	0.0038	1.23	-0.00242	-0.00089	0.75
865_1613	-7.8	0.0010	1.01	-0.00036	-0.00031	0.97
865_2200	-6.1	0.0011	1.01	-0.00028	-0.00023	0.96
664						
1613_2200	-135.9	0.0029	1.96	-0.00263	-0.00085	0.37
865_1613	-36.3	0.0007	1.09	-0.00056	-0.00039	0.92
865_2200	-33.8	0.0006	1.09	-0.0005	-0.00033	0.90

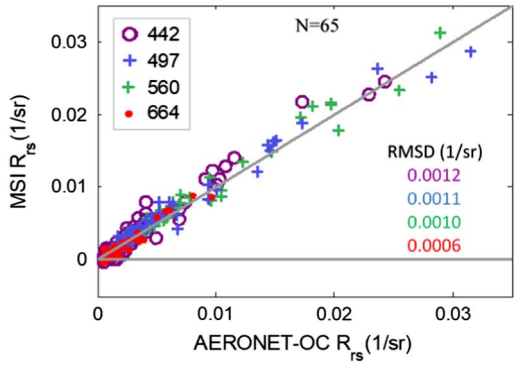

Fig. 6. Scatterplot of AERONET-OC $R_{rs}(\lambda)$ measurements versus $R_{rs}(\lambda)$ derived from Sentinel-2A (MSI) processed via SeaDAS after vicarious calibration. The MSI-derived R_{rs} have become more consistent with in situ following implementations of the vicarious calibration gains.

effects (Bulgarelli et al., 2014), which together result in noisy matchups (Pahlevan et al., 2016). Both of these effects are due to large footprint sizes. In addition, large angular observations of each OC measurement carries larger uncertainties than those associated with the near-nadir MSI (or OLI) measurements (Pahlevan et al., 2017b). Here, we further discuss factors that contribute to inaccuracies present in MSI products that are not captured in the matchup analyses (Fig. 6).

Through the SNR analyses, we demonstrated that the MSI-derived R_{rs} products (i.e., 497, 560, 664) require spatial aggregations to 20 or 30 m to yield reasonably smooth products comparable to those of OLI for typical TOA radiances tabulated in Table 1. Such spatial aggregation schemes may seem necessary when cross-mission (MSI-OLI) product consistency is desired. Note, however, that MSI and OLI SNRs are still considerably below the radiometric requirements recommended (e.g., SNR(443) = 1000) for existing (Hu et al., 2012) and/or future (Del Castillo et al., 2012) ocean color missions. Fig. 8 provides visual inspections of the noise (and/or striping) in the MSI- and OLI-derived R_{rs} (blue) products showing Po Rive (Italy) discharging into Adriatic Sea. Similar to the procedure described in Section 3, spatial aggregations were carried out for processing both MSI and OLI data (Pahlevan et al., 2017a; Vanhellemont and Ruddick, 2015). By inspecting the areas in the open sea, it is evident that there is more striping associated with the MSI products than that of the OLI. Such noise sources and the resulting discrepancies in the products are less pronounced over very turbid inland waters (see inland waters in R_{rs} (497) products).

Furthermore, although we showed that the vicarious calibration gain coefficients reduced the biases for the MSI-derived R_{rs} products (Table 2 versus Table 4), large uncertainties exist for these gains (Table 3). This is primarily due to the lack of adequate suitable vicarious matchups. In addition, Bailey et al. (2008) reported higher uncertainties associated with long-term gains derived using the BOUSSOLE observations than those derived through MOBY measurements.

Another source of uncertainty in R_{rs} products, in particular in the blue bands, are the errors in the atmospheric correction. Regardless of how well the gaseous absorptions are accounted for, the errors in aerosol removals dominate the total uncertainty budget. Pahlevan et al. (2017a) showed that if the ambient aerosol properties are not represented in the aerosol models (Ahmad et al., 2010), high uncertainties in R_{rs}(443) are expected. It is, thus, necessary to augment/update the existing aerosol models (Ahmad et al., 2010) to reduce the associated noise when retrieving R_{rs} over inland waters, in particular, those with high loads of dissolved organic matters.

Table 4
The statistical analyses of the MSI-derived matchups (R_{rs}) after implementing vicarious calibration gains. The values correspond to the aerosol removal using the 865–1613 nm band combination. Comparing to the given values in Table 2, RD, RMSD, and biases are considerably reduced.

Bands	*RD(%)*	*RMSD (1/sr)*	Slope	Intercept	Bias (1/sr)	R^2
442	− 4.61	0.0012	1.11	− 0.0002	0.0003	0.95
497	6.04	0.0011	0.97	0.0003	0.0002	0.97
560	5.68	0.0010	1.03	0.0001	0.0003	0.97
664	− 24.01	0.0006	1.10	− 0.0004	− 0.0002	0.92

One common issue associated with both MSI and OLI data products is the lack of accuracy in the removal of residual sun glint. The odd and even detector modules (or focal plane modules; FPM) are located on the two sides of the primary optical axis (Kudryavtsev et al., 2017; Markham et al., 2014); thus, one module is forward-looking (sensor and sun on the same side of the target pixel) and the other is the aft-looking, which directly looks into the partially sunglint region. These impacts are discernable when the solar zenith angle (SZA) is low. This effect is more pronounced towards the east edge of the swaths and under hazy conditions (reflected solar radiation off of heavy aerosol loads). In general, sunglint is more pronounced in MSI imagery than that for OLI because Sentinel-2A's equatorial crossing time is ~30 min after Landsat-8, resulting in higher solar elevation angles and increased sun glitter (Drusch et al., 2012; Irons et al., 2012). Currently, per-pixel and per-band Fresnel correction is incorporated in SeaDAS as part of the Rayleigh contribution removal; however, the correction is yet to be implemented for the aerosol removal. Furthermore, it has been shown that spatial nonuniformities across the swath, i.e., module-to-module, and within each module exist at low radiance levels for the OLI (Pahlevan et al., 2017b). Similar nonuniformities may also exist for MSI requiring further corrections (see R_{rs} (497) in Fig. 2) for more consistent products.

As pointed out in Section 3, we have incorporated a broadband to narrowband conversion in the R_{rs} production. Nevertheless, there is still a need for shifting the modeled narrowband R_{rs} to the band centers of the in situ radiometers (Zibordi et al., 2006). Although the impact on the matchup analyses may be small, further research is required to enable per-matchup spectral adjustments for such differences when evaluating MSI (or OLI) products (Mélin and Sclep, 2015). Furthermore, the methodology currently applied for the removal of the NIR water-leaving radiances (Bailey et al., 2010) may not be applicable to

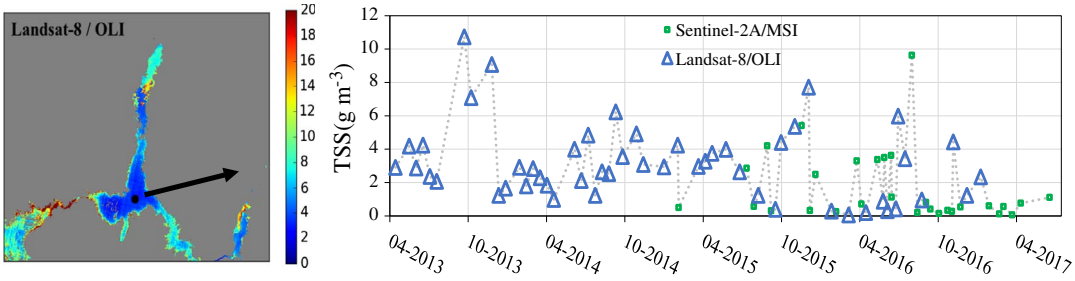

Fig. 7. shows a time-series of Landsat-8- and Sentinel-2A-derived TSS products for an area (denoted with a filled circle to the left) in the central basin of Lake Mead, Nevada, USA. The MSI-derived products improve the frequency of Landsat-8 observations. The anomalous water conditions (i.e., high TSS loads) can be inferred from the plot. The products are found relatively consistent across the two missions.

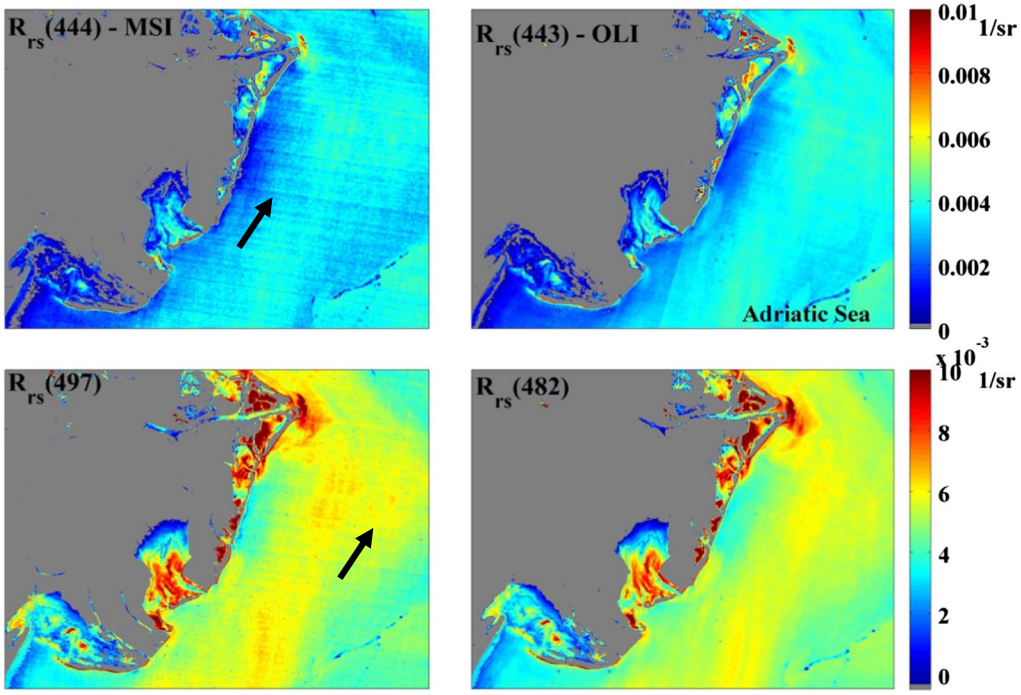

Fig. 8. The R_{rs} products associated with the blue bands derived from MSI and OLI images collected near simultaneously on August 4th 2016 over the western Adriatic Sea nearby Po River discharge. It is evident that the MSI products show more noise than those of OLI over the open sea. Cross-track striping is indicated by the arrows in Sentinel-2A products. The impact of instrument noise is not as pronounced over inland waters. Note that the MSI products have been vicariously calibrated using the preliminary gains (Table 3). Also the MSI and OLI products are shown on 20 and 30 m grid cell and aerosol correction has been performed using average Rayleigh-corrected radiances computed for blocks of 180 × 180 m (i.e., 9 × 9- and 6 × 6-elment windows). (For interpretation of the references to color in this figure legend, the reader is referred to the web version of this article.)

typically turbid/trophic nearshore coastal and inland waters; thus, future revisions of this approach seem necessary. Adjacency effects (Santer and Schmechtig, 2000) for bodies of waters surrounded by steep topography or adjacent to very bright targets (e.g., ice) (Bélanger et al., 2007) can also be considered another area of research. In general, there is a need for extensive intercomparisons of various atmospheric correction methods for nearshore coastal and inland water applications. For example, Dörnhöfer et al. (2016) and Martins et al. (2017) performed preliminary analyses of different atmospheric corrections methods for limited number of MSI imagery. In future, such multi-processing validation exercises should be extended in space and time, and for various aquatic applications.

8. Summary & conclusion

This manuscript provides the descriptions of our SeaDAS implementations of Sentinel-2A MSI (Level-1C) data processing and the associated qualitative and quantitative validations of the remote sensing reflectance (R_{rs}) products, which are critical for the retrievals of water constituents products like the concentrations of total suspended solids (TSS). The quality of products went under scrutiny by comparisons with the OLI-derived products and with the AERONET-OC in situ radiometric data. With radiometric performances, comparable to those of OLI (onboard Landsat-8), it was shown that high-quality products can be derived from MSI data. Further, vicarious calibrations using the BOUSSOLE data helped minimize the overall biases observed in the preliminary matchup analyses carried out using the AERONET-OC data. A time-series of TSS products derived from combined Landsat-8 and Sentinel-2A imagery further demonstrated the coherence of the data products. While the MSI R_{rs} products are found to be mostly consistent with those of OLI and with the AERONET-OC measurements, a full evaluation of the performance requires a community-wide effort to ensure high-quality cross-mission products under various atmospheric conditions and for different aquatic systems (in particular inland waters). We suggest several avenues for future research and developments, including improvements in atmospheric corrections over extremely CDOM-rich or turbid waters, tackling with residual sunglint under hazy conditions, and improving methods for accounting for differences in the spectral bands for validation practices. By providing consistent multi-mission R_{rs} products from Landsat-Sentinel-2A/B constellation, the science community will be able to devise suitable algorithms for the retrievals of biogeochemical properties in coastal/inland waters for operational uses and decision-making activities.

Acknowledgement

The authors are grateful to Jim Storey of the Landsat cal/val team for providing the code creating per-pixel angle coefficients. We also would like to thank Sean Bailey for his insights for the implementation of the MSI processing into SeaDAS as well as Sandeep Chittimalli with the Terrestrial Information Systems lab at NASA Goddard Space Flight Center for his contributions to this manuscript. The authors are grateful to the BOUSSOLE project for maintaining and providing high-quality hyperspectral in situ data for preliminary vicarious calibration of Sentinel-2A MSI data. BOUSSOLE is funded by the European space agency (ESA) and the French space agency (CNES), and is supported by the French Institut National des Sciences de l'Univers (INSU). We appreciate the Principle Investigators of the AERONET-OC for the maintenance and distribution of data to the community. These include Giuseppe Zibordi, Alex Gilerson and Samir Ahmad, Timothy Moore, Alan Wideman, Bill Gibson, Robert Arnone, Susanne Kratzer, and Dimitry Van der Zande. Pahlevan is funded by the NASA grant # NNX16AI16G under the New Investigator Program (NIP). We also thank Quinten Vanhellemont for sharing the latest updates of Nechad et al. (2010) algorithm coefficients and appreciate three anonymous reviewers for their thoughtful and constructive comments.

Appendix A. Below is a full description of the step-by-step procedure for generating 10, 20, and 60 m angle coefficients for processing Sentinel-2A (S2A) imagery in SeaDAS. The Python code available for each step in noted as appropriate

1. Read the viewing angle values in the tile metadata (XML) file and convert them to observations of directions to the spacecraft in geocentric coordinates (i.e., get_angleobs).
   a. Read the valid viewing angle fields from the tile metadata XML file, labelling them by band and detector module.
   b. Each angle observation contains: band ID, detector module ID,

UTM X coordinate of ground point, UTM Y coordinate of ground point, unit vector (in Earth centered coordinates) pointing from ground point to satellite, geocentric vector to the ground point.

i. The angle observation's UTM X/Y ground location is computed from the index in the metadata array, the 5000 m metadata grid spacing, and the tile upper left corner UTM coordinates.
ii. The UTM X/Y coordinates are converted to latitude, longitude using the UTM projection equations.
iii. Latitude and longitude are used to compute the geocentric Earth vector based upon the WGS84 Earth ellipsoid.
iv. The viewing azimuth and zenith angles are used to construct the satellite viewing vector in non-local space rectangular (LSR) coordinates.

2. Reconstruct the S2A orbit from the viewing angle observations (i.e., Fit_Orbit) and calculate a time of observation for each input angle.
   a. Construct a nominal circular sun-synchronous orbit model using the nominal S2A orbital radius, inclination, and period. This model assumes constant orbital radius and uniform precession to maintain a pseudo-inertial sun-synchronous orbit. Instead of orbit angle from the equator (central travel angle) and equatorial crossing longitude as the other two orbit parameters used the geocentric latitude and longitude of an orbit reference point used as the time origin of the simple orbit model.
      i. For each observation:
         1. Append a time of observation field (initialized to zero).
         2. Project the ground-to-satellite vector from the ground point coordinates out to the point where the sum of the ground vector and viewing vector has a magnitude equal to the nominal orbital radius.
         3. Calculate the geocentric latitude and longitude of this projected point.
      ii. Calculate the average of these geocentric latitude and longitude values for all observations.
   b. Perform a (linearized) least squares fit to the angle vector observations by adjusting the four orbit parameters and the time of observation (relative to the orbit origin) for each viewing vector.
      i. Partial derivatives for each orbital parameter and for the time of observation are computed numerically.
      ii. The time parameters are forward eliminated as each observation is processed and then calculated by back substitution once the orbit parameter corrections have been evaluated.
      iii. For the first iteration, the orbit corrections are set to zero and only the time parameters are evaluated. This allows the time values (initially set at zero) to adjust to reasonable values without distorting the orbit model.
      iv. The iterations continue until the total orbit parameter adjustments (scaled to nominal meters at the Earth's surface) and the root-mean-square time corrections have both converged to within acceptable thresholds.
      v. The final fitted orbit parameters: latitude, longitude, radius, and inclination; the final orbit parameter adjustment (in meters), the final RMS time adjustment (in seconds), and the RMS viewing angle observation residual are presented to the user.
   c. As an efficiency measure, evaluate the orbit model (i.e., generate a geocentric X, Y, Z position) every 100 microseconds starting 1 s before the first angle observation and ending 1 s after the last angle observation. The resulting look up table will be used to accelerate the generation of satellite positions as a function of time with a precision better than 1 m.
3. Use the calculated observation times to construct a line/sample vs. time model for each band and detector that had valid viewing angle data (i.e., Fit_Time). This will make it possible to relate tile line/sample coordinates to the orbit model when constructing new viewing vectors.
   a. For band/detector combinations that have plenty of angle observations this is straightforward. Simply fit a four parameter polynomial model mapping the UTM X and Y offsets from the tile upper left corner to time of observation.
   b. There will typically be several detectors and detector modules that do not contribute to the current tile and so there will be no angle observations in the metadata. This is not really a problem since we will not need to generate new angles for these detectors either.
4. Read the detector footprint coordinates from the quality indicator (QI) files (i.e., get_detfootprint). These footprints consist of lists of UTM X/Y pairs defining closed polygons that delineate the coverage of each detector in each band which contributes to the tile. The Python XML parsing routines are used to extract these polygon coordinates.
5. As an efficiency measure, pre-calculate the geocentric position vectors for every output location for which a new set of viewing angles is desired (CalcGroundVectors). Three sets of vectors are calculated, one for the 60 m bands, one for the 20 m bands, and one for the 10 m bands, taking into account the user defined subsampling ratio. These positions are calculated at the pixel center locations.
6. Generate the angle band files for each spectral band.

Appendix B. Supplementary data

Supplementary data to this article can be found online at http://dx.doi.org/10.1016/j.rse.2017.08.033.

References

Ahmad, Z., Fraser, R.S., 1982. An iterative radiative transfer code for ocean-atmosphere systems. J. Atmos. Sci. 39, 656–665.

Ahmad, Z., Franz, B.A., McClain, C.R., Kwiatkowska, E.J., Werdell, J., Shettle, E.P., Holben, B.N., 2010. New aerosol models for the retrieval of aerosol optical thickness and normalized water-leaving radiances from the SeaWiFS and MODIS sensors over coastal regions and open oceans. Appl. Opt. 49, 5545–5560.

Antoine, D., d'Ortenzio, F., Hooker, S.B., Bécu, G., Gentili, B., Tailliez, D., Scott, A.J., 2008a. Assessment of uncertainty in the ocean reflectance determined by three satellite ocean color sensors (MERIS, SeaWiFS and MODIS-A) at an offshore site in the Mediterranean Sea (BOUSSOLE project). J. Geophys. Res. Oceans 113.

Antoine, D., Guevel, P., Deste, J.-F., Bécu, G., Louis, F., Scott, A.J., Bardey, P., 2008b. The "BOUSSOLE" buoy-a new transparent-to-swell taut mooring dedicated to marine optics: Design, tests, and performance at sea. J. Atmos. Ocean. Technol. 25, 968–989.

Bailey, S.W., Werdell, P.J., 2006. A multi-sensor approach for the on-orbit validation of ocean color satellite data products. Remote Sens. Environ. 102, 12–23.

Bailey, S.W., Hooker, S.B., Antoine, D., Franz, B.A., Werdell, P.J., 2008. Sources and assumptions for the vicarious calibration of ocean color satellite observations. Appl. Opt. 47, 2035–2045.

Bailey, S.W., Franz, B.A., Werdell, P.J., 2010. Estimation of near-infrared water-leaving reflectance for satellite ocean color data processing. Opt. Express 18, 7521–7527.

Bélanger, S., Ehn, J.K., Babin, M., 2007. Impact of sea ice on the retrieval of water-leaving reflectance, chlorophyll a concentration and inherent optical properties from satellite ocean color data. Remote Sens. Environ. 111, 51–68.

Bulgarelli, B., Kiselev, V., Zibordi, G., 2014. Simulation and analysis of adjacency effects in coastal waters: a case study. Appl. Opt. 53, 1523–1545.

Cao, C., Weinreb, M., Xu, H., 2004. Predicting simultaneous nadir overpasses among polar-orbiting meteorological satellites for the intersatellite calibration of radiometers. J. Atmos. Ocean. Technol. 21, 537–542.

Clark, D.K., Yarbrough, M.A., Feinholz, M., Flora, S., Broenkow, W., Kim, Y.S., Johnson, B.C., Brown, S.W., Yuen, M., Mueller, J.L., 2003. MOBY, a radiometric buoy for performance monitoring and vicarious calibration of satellite ocean color sensors: measurement and data analysis protocols. In: Ocean Optics Protocols for Satellite Ocean Color Sensor Validation, Revision. 4. pp. 3–34.

Del Castillo, C., Platnick, S., Antoine, D., 2012. In: Del Castillo, C., Platnick, S., Antoine, D., NASA (Eds.), Pre-Aerosol, Clouds, and ocean Ecosystem (PACE) Mission Science Definition Team Report, . http://decadal.gsfc.nasa.gov/pace_documentation/PACE_SDT_Report_final.pdf.

D'Odorico, P., Gonsamo, A., Damm, A., Schaepman, M.E., 2013. Experimental evaluation of Sentinel-2 spectral response functions for NDVI time-series continuity. IEEE Trans. Geosci. Remote Sens. 51, 1336–1348.

Dörnhöfer, K., Göritz, A., Gege, P., Pflug, B., Oppelt, N., 2016. Water constituents and water depth retrieval from Sentinel-2a—a first evaluation in an oligotrophic lake. Remote Sens. 8, 941.

Drusch, M., Del Bello, U., Carlier, S., Colin, O., Fernandez, V., Gascon, F., Hoersch, B.,

Isola, C., Laberinti, P., Martimort, P., 2012. Sentinel-2: ESA's optical high-resolution mission for GMES operational services. Remote Sens. Environ. 120, 25–36.
Franz, B.A., Bailey, S.W., Werdell, P.J., McClain, C.R., 2007. Sensor-independent approach to the vicarious calibration of satellite ocean color radiometry. Appl. Opt. 46, 5068–5082.
Franz, B.A., Bailey, S.W., Kuring, N., Werdell, P.J., 2015. Ocean color measurements with the Operational Land Imager on Landsat-8: implementation and evaluation in SeaDAS. J. Appl. Remote. Sens. 9, 096070.
Gatti, A., Bertolini, A., 2013. Sentinel-2 products specification document. Available online. https://earth/.esa.int/documents/247904/685211/Sentinel-2+Products+Specification+Document, Accessed date: 23 February 2015.
Gerace, A.D., Schott, J.R., Nevins, R., 2013. Increased potential to monitor water quality in the near-shore environment with Landsat's next-generation satellite. J. Appl. Remote. Sens. 7, 073558.
Gordon, H.R., 1990. Radiometric considerations for ocean color remote sensors. Appl. Opt. 29, 3228–3236.
Gordon, H.R., 1998. In-orbit calibration strategy for ocean color sensors. Remote Sens. Environ. 63, 265–278.
Gordon, H.R., Wang, M., 1994. Retrieval of water-leaving radiance and aerosol optical thickness over the oceans with SeaWiFS: a preliminary algorithm. Appl. Opt. 33, 443–452.
Goyens, C., Jamet, C., Schroeder, T., 2013. Evaluation of four atmospheric correction algorithms for MODIS-Aqua images over contrasted coastal waters. Remote Sens. Environ. 131, 63–75.
Hu, C., Feng, L., Lee, Z., Davis, C.O., Mannino, A., McClain, C.R., Franz, B.A., 2012. Dynamic range and sensitivity requirements of satellite ocean color sensors: learning from the past. Appl. Opt. 51, 6045–6062.
IOCCG, 2000. Remote Sensing of Ocean Colour in Coastal, and Other Optically-Complex, Waters. IOCCG S. Sathyendranath Dartmouth, Canada.
Irons, J.R., Dwyer, J.L., Barsi, J.A., 2012. The next Landsat satellite: the Landsat Data Continuity Mission. Remote Sens. Environ. 122, 11–21.
Knight, E., 2017. OLI design trades and the advantages for aquatic science studies. In: Ball Aerospace.
Kudryavtsev, V., Yurovskaya, M., Chapron, B., Collard, F., Donlon, C., 2017. Sun glitter imagery of ocean surface waves. Part 1: directional spectrum retrieval and validation. J. Geophys. Res. Oceans 122, 1369–1383.
Kutser, T., Paavel, B., Verpoorter, C., Ligi, M., Soomets, T., Toming, K., Casal, G., 2016. Remote sensing of black lakes and using 810 nm reflectance peak for retrieving water quality parameters of optically complex waters. Remote Sens. 8, 497.
Lee, Z., Shang, S., Lin, G., Chen, J., Doxaran, D., 2016. On the modeling of hyperspectral remote-sensing reflectance of high-sediment-load waters in the visible to shortwave-infrared domain. Appl. Opt. 55, 1738–1750.
Liu, H., Li, Q., Shi, T., Hu, S., Wu, G., Zhou, Q., 2017. Application of sentinel 2 MSI images to retrieve suspended particulate matter concentrations in Poyang Lake. Remote Sens. 9, 761.
Markham, B., Barsi, J., Kvaran, G., Ong, L., Kaita, E., Biggar, S., Czapla-Myers, J., Mishra, N., Helder, D., 2014. Landsat-8 operational land imager radiometric calibration and stability. Remote Sens. 6, 12275–12308.
Martins, V.S., Barbosa, C.C.F., de Carvalho, L.A.S., Jorge, D.S.F., Lobo, F.d.L., & Novo, E.M.L.d.M., 2017. Assessment of atmospheric correction methods for sentinel-2 MSI images applied to amazon floodplain lakes. Remote Sens. 9, 322.
Mélin, F., Sclep, G., 2015. Band shifting for ocean color multi-spectral reflectance data. Opt. Express 23, 2262–2279.
Meygret, A., Baillarin, S., Gascon, F., Hillairet, E., Dechoz, C., Lacherade, S., Martimort, P., Spoto, F., Henry, P., Duca, R., 2009. SENTINEL-2 image quality and level 1 processing. In: SPIE Optical Engineering + Applications. International Society for Optics and Photonics (pp. 74520D-74520D-74510).
Mobley, C.D., Werdell, J., Franz, B., Ahmad, Z., & Bailey, S. (2016). Atmospheric Correction for Satellite Ocean Color Radiometry. Mobley, C.D., Werdell, J., Franz, B., Ahmad, Z., & Bailey, S. NASA/TM-2016-217551, GSFC-E-DAA-TN35509.
Moses, W.J., Gitelson, A.A., Berdnikov, S., Povazhnyy, V., 2009. Satellite estimation of chlorophyll-a concentration using the red and NIR bands of MERIS-2014; The Azov sea case study. IEEE Geosci. Remote Sens. Lett. 6, 845–849.
Nechad, B., Ruddick, K., Park, Y., 2010. Calibration and validation of a generic multi-sensor algorithm for mapping of total suspended matter in turbid waters. Remote Sens. Environ. 114, 854–866.
Pahlevan, N., Schott, J., 2013. Leveraging EO-1 to Evaluate Capability of New Generation of Landsat Sensors for Coastal/Inland Water Studies. IEEE J. Sel. Topics Appl. Earth Observ. Rem. Sens. 6, 360–374.
Pahlevan, N., Lee, Z., Hu, C., Schott, J.R., 2014a. Diurnal remote sensing of coastal/oceanic waters: a radiometric analysis for Geostationary Coastal and Air Pollution Events. Appl. Opt. 53, 648–665.
Pahlevan, N., Lee, Z., Wei, J., Schaff, C., Schott, J., Berk, A., 2014b. On-orbit radiometric characterization of OLI (Landsat-8) for applications in aquatic remote sensing. Remote Sens. Environ. 154, 272–284.
Pahlevan, N., Sarkar, S., Franz, B.A., 2016. Uncertainties in coastal ocean color products: Impacts of spatial sampling. Remote Sens. Environ. 181, 14–26.
Pahlevan, N., Roger, J.-C., Ahmad, Z., 2017a. Revisiting short-wave-infrared (SWIR) bands for atmospheric correction in coastal waters. Opt. Express 25, 6015–6035.
Pahlevan, N., Schott, J.R., Franz, B.A., Zibordi, G., Markham, B., Bailey, S., Schaaf, C.B., Ondrusek, M., Greb, S., Strait, C.M., 2017b. Landsat 8 remote sensing reflectance (R rs) products: evaluations, intercomparisons, and enhancements. Remote Sens. Environ. 190, 289–301.
Santer, R., Schmechtig, C., 2000. Adjacency effects on water surfaces: primary scattering approximation and sensitivity study. Appl. Opt. 39, 361–375.
Schott, J.R., 2007. Remote Sensing The Image Chain Approach, 2nd ed. Oxford Unversity Press, New York.
Segl, K., Guanter, L., Gascon, F., Kuester, T., Rogass, C., Mielke, C., 2015. S2eteS: an end-to-end modeling tool for the simulation of Sentinel-2 image products. IEEE Trans. Geosci. Remote Sens. 53, 5560–5571.
Siegel, D.A., Wang, M., Maritorena, S., Robinson, W., 2000. Atmospheric correction of satellite ocean color imagery: the black pixel assumption. Appl. Opt. 39, 3582–3591.
Toming, K., Kutser, T., Laas, A., Sepp, M., Paavel, B., Nõges, T., 2016. First experiences in mapping lake water quality parameters with Sentinel-2 MSI imagery. Remote Sens. 8, 640.
Vanhellemont, Q., Ruddick, K., 2015. Advantages of high quality SWIR bands for ocean colour processing: Examples from Landsat-8. Remote Sens. Environ. 161, 89–106.
Wang, M., Shi, W., 2007. The NIR-SWIR combined atmospheric correction approach for MODIS ocean color data processing. Opt. Express 15, 15722–15733.
Wang, M., Wei, S., 2012. Sensor noise effects of the SWIR bands on MODIS-derived ocean color products. IEEE Trans. Geosci. Remote Sens. 50, 3280–3292.
Wang, M., Franz, B.A., Barnes, R.A., McClain, C.R., 2001. Effects of spectral bandpass on SeaWiFS-retrieved near-surface optical properties of the ocean. Appl. Opt. 40, 343–348.
Zibordi, G., Holben, B., Hooker, S.B., Mélin, F., Berthon, J.-F., Slutsker, I., Giles, D., Vandemark, D., Feng, H., Rutledge, K., Schuster, G., Al Mandoos, A., 2006. A network for standardized ocean color validation measurements. EOS Trans. Am. Geophys. Union 87, 293–297.
Zibordi, G., Berthon, J.-F., Mélin, F., D'Alimonte, D., Kaitala, S., 2009. Validation of satellite ocean color primary products at optically complex coastal sites: Northern Adriatic Sea, Northern Baltic Proper and Gulf of Finland. Remote Sens. Environ. 113, 2574–2591.